nature genetics

Spatial heterogeneity in medulloblastoma

A Sorana Morrissy[1,2,37], Florence M G Cavalli[1,2,37], Marc Remke[1–5,37], Vijay Ramaswamy[1,2,6], David J H Shih[1,2,7], Borja L Holgado[1,2], Hamza Farooq[1,2,7], Laura K Donovan[1,2], Livia Garzia[1,2,8], Sameer Agnihotri[9], Erin N Kiehna[10], Eloi Mercier[11], Chelsea Mayoh[11], Simon Papillon-Cavanagh[12], Hamid Nikbakht[12], Tenzin Gayden[12], Jonathon Torchia[2,6,7], Daniel Picard[3–5], Diana M Merino[2,6,13], Maria Vladoiu[1,2], Betty Luu[1,2], Xiaochong Wu[1,2], Craig Daniels[1,2], Stuart Horswell[14], Yuan Yao Thompson[1,2,7], Volker Hovestadt[15], Paul A Northcott[16], David T W Jones[16], John Peacock[1,2,7], Xin Wang[1,2,7], Stephen C Mack[1,2,7], Jüri Reimand[17–19], Steffen Albrecht[20], Adam M Fontebasso[21], Nina Thiessen[11], Yisu Li[11], Jacqueline E Schein[11], Darlene Lee[11], Rebecca Carlsen[11], Michael Mayo[11], Kane Tse[11], Angela Tam[11], Noreen Dhalla[11], Adrian Ally[11], Eric Chuah[11], Young Cheng[11], Patrick Plettner[11], Haiyan I Li[11], Richard D Corbett[11], Tina Wong[11], William Long[11], James Loukides[2], Pawel Buczkowicz[22], Cynthia E Hawkins[2,22], Uri Tabori[2,6], Brian R Rood[23], John S Myseros[24], Roger J Packer[25], Andrey Korshunov[26], Peter Lichter[15,27], Marcel Kool[16], Stefan M Pfister[16,27,28], Ulrich Schüller[29–31], Peter Dirks[2,10], Annie Huang[2,6], Eric Bouffet[2,6], James T Rutka[2,7,10], Gary D Bader[19], Charles Swanton[32,33], Yusanne Ma[11], Richard A Moore[11], Andrew J Mungall[11], Jacek Majewski[21], Steven J M Jones[11,34,35], Sunit Das[1,2,36], David Malkin[6], Nada Jabado[21], Marco A Marra[11,34] & Michael D Taylor[1,2,7]

Spatial heterogeneity of transcriptional and genetic markers between physically isolated biopsies of a single tumor poses major barriers to the identification of biomarkers and the development of targeted therapies that will be effective against the entire tumor. We analyzed the spatial heterogeneity of multiregional biopsies from 35 patients, using a combination of transcriptomic and genomic profiles. Medulloblastomas (MBs), but not high-grade gliomas (HGGs), demonstrated spatially homogeneous transcriptomes, which allowed for accurate subgrouping of tumors from a single biopsy. Conversely, somatic mutations that affect genes suitable for targeted therapeutics demonstrated high levels of spatial heterogeneity in MB, malignant glioma, and renal cell carcinoma (RCC). Actionable targets found in a single MB biopsy were seldom clonal across the entire tumor, which brings the efficacy of monotherapies against a single target into question. Clinical trials of targeted therapies for MB should first ensure the spatially ubiquitous nature of the target mutation.

Many cancer types show considerable intertumoral heterogeneity between individuals[1–3]. Molecular biomarkers are intended to (i) tailor treatment intensities[4,5], (ii) define oncogenic drivers for targeted therapies[5–7], and (iii) identify diagnostic mutations (e.g., *SMARCB1* mutations in atypical teratoid/rhabdoid tumors)[8]. Currently, clinical diagnoses are based on single biopsies, with the assumption of spatial homogeneity across tumors; however, spatial heterogeneity could lead to erroneous tumor classification or the selection of therapies against targets that are present only in a locally restricted portion of the tumor. These implications were recently highlighted in late-stage RCC[9,10], with highly divergent mutational profiles affecting *MTOR* and *TP53*, as well as demonstrating good and poor prognostic gene signatures in multiregion biopsies from the same tumor[10,11].

To determine the degree and clinical importance of spatial heterogeneity in MB, we performed multiregional biopsies and compared gene expression profiles, DNA copy-number alterations (CNAs), and somatic mutations. Our cohort included 9 primary MBs, 16 HGGs (10 with gene expression only[12]), and 10 RCCs[10], with 4–11 spatially distinct biopsies from each (median: 6). An overview of the data types available for each patient is presented in **Supplementary Table 1a** and **Supplementary Figure 1**.

Glioblastoma[13] and MB[14] each comprise four distinct molecular subgroups that are discerned through analysis of transcriptional data. Unsupervised hierarchical clustering (HCL) of expression data has shown that MB biopsies form tight clusters apart from single samples[15–20] (8/8; **Fig. 1a**, **Supplementary Fig. 2a**,**b**), whereas in HGGs (3/3) and RCCs (8/9), multiregion biopsies from single individuals clustered apart when combined with single samples (**Supplementary Fig. 2c–f**). Overall, on the basis of the s.d. of expression, intertumoral differences were greater than intratumoral heterogeneity in each tumor type (**Fig. 1b**). Subtype prediction with Predictive Analysis of Microarrays (PAM) showed that 21% (13/63) of glioblastoma multiregion samples diverged from the most commonly observed subtype for each patient, compared with only 2% (1/52) of MB biopsies ($P = 0.003$; **Fig. 1c–e**, **Supplementary Figs. 3–6**). When we considered only

A full list of affiliations appears at the end of the paper.

Received 3 November 2014; accepted 17 March 2017; published online 10 April 2017; doi:10.1038/ng.3838

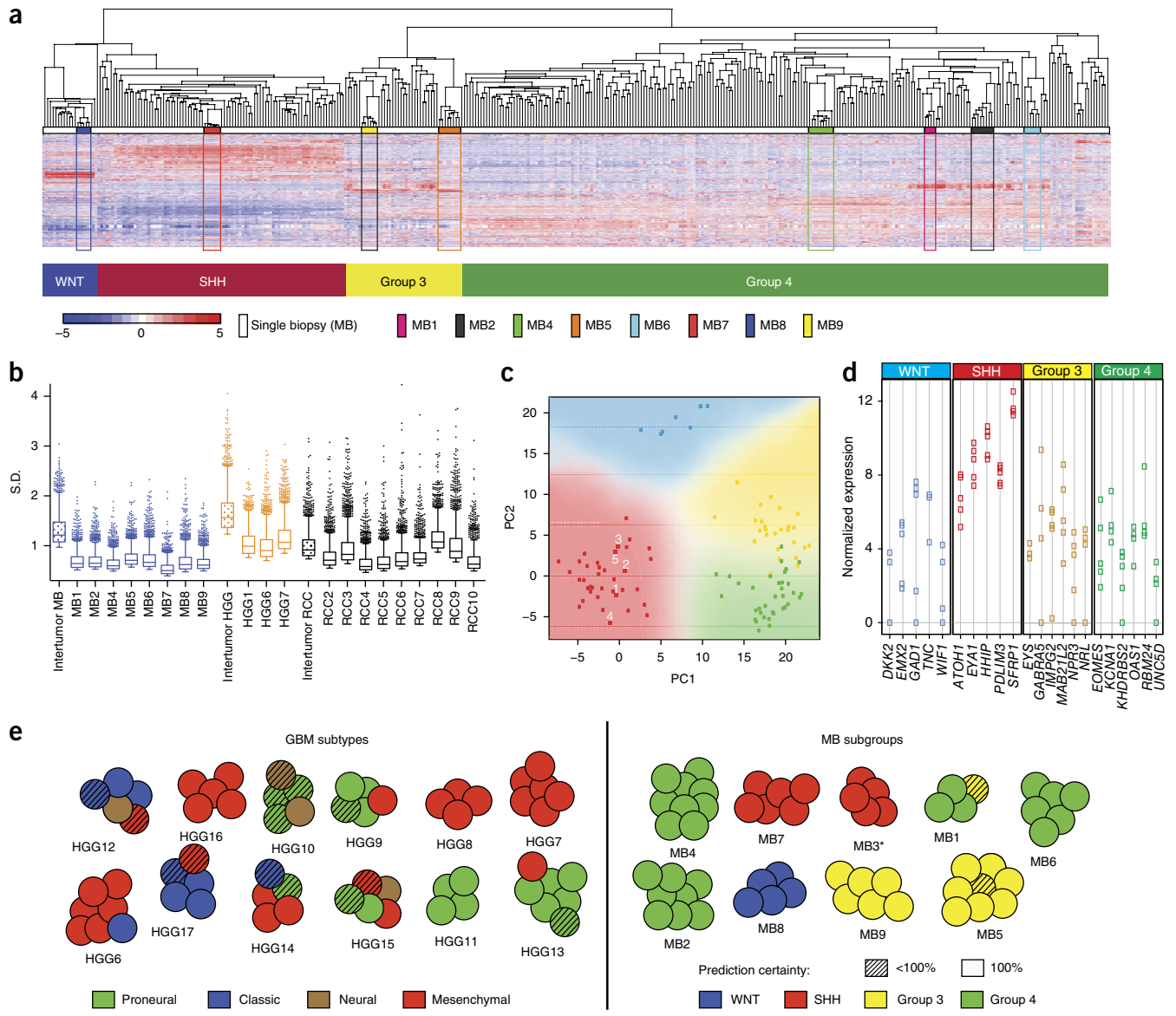

Figure 1 Medulloblastomas, but not glioblastomas, show reliable transcriptome-based subgroup prediction. (**a**) Unsupervised HCL using 1,000 high-s.d. transcripts of eight multiregion MB samples combined with single biopsies ($n = 334$) demonstrates tight clustering of matched multiregion MB samples across subgroups. (**b**) The top 2,000 s.d.-transcript values determined on intra- and intertumor levels in MB, HGG, and RCC samples. Center lines indicate data medians; box limits indicate the 25th and 75th percentiles; whiskers extend 1.5 times the interquartile range from the 25th and 75th percentiles; outliers are represented by individual points. Intertumoral and intratumoral values are indicated by patterned and white boxes, respectively. (**c**) Principal component analysis (PCA) of 22 MB subgroup marker genes confirmed a low degree of transcriptional intratumoral heterogeneity, exemplified in MB3. Multiregion biopsy numbers of MB3 are indicated in the red-shaded region of the plot. PCA was conducted with 103 single-biopsy samples analyzed by NanoString. (**d**) Dot plot illustrating highly similar marker-gene expression in all multiregion biopsies for MB3. (**e**) Glioblastoma (GBM) subtype and MB subgroup predictions based on PAM results. The SHH subgroup affiliation of MB3 (marked with an asterisk) was inferred from NanoString results. Hashed circles indicate biopsies with <100% prediction certainty.

biopsies with subgroup predictions of 100% confidence, we found that all MB tumors had concordant subgroup calls between multiple biopsies (9/9), compared with only 55% of glioblastomas (6/11; $P = 0.038$; **Fig. 1e**). We conclude that MB can be robustly and reliably subgrouped from only a single biopsy, but glioblastoma cannot.

We identified somatic CNAs by using a custom pipeline based on the TITAN algorithm[21], which is robust to high levels of normal contamination (Online Methods). Regions of CNA were identified in all three tumor types (**Fig. 2a**, **Supplementary Figs. 7** and **8**, **Supplementary Table 1b**,**c**), and unsupervised HCL of clonal segments showed tight clustering of individual biopsies in the cohort across all tumor entities (**Fig. 2b**, **Supplementary Fig. 9**). CNA-derived measurements of spatial heterogeneity highlighted the variance between individuals for each tumor type (**Fig. 2c**). Somatic single-nucleotide variants (SNVs) and insertions/deletions (indels) recapitulated a similar pattern of spatial heterogeneity across tumors (**Fig. 2d**, **Supplementary Table 1d**). Overall, on the basis of the mutation and CNA data, none of the three tumor types comprised only homogeneous or heterogeneous tumors; rather, each had a repertoire of tumors residing along a continuum of genetic heterogeneity.

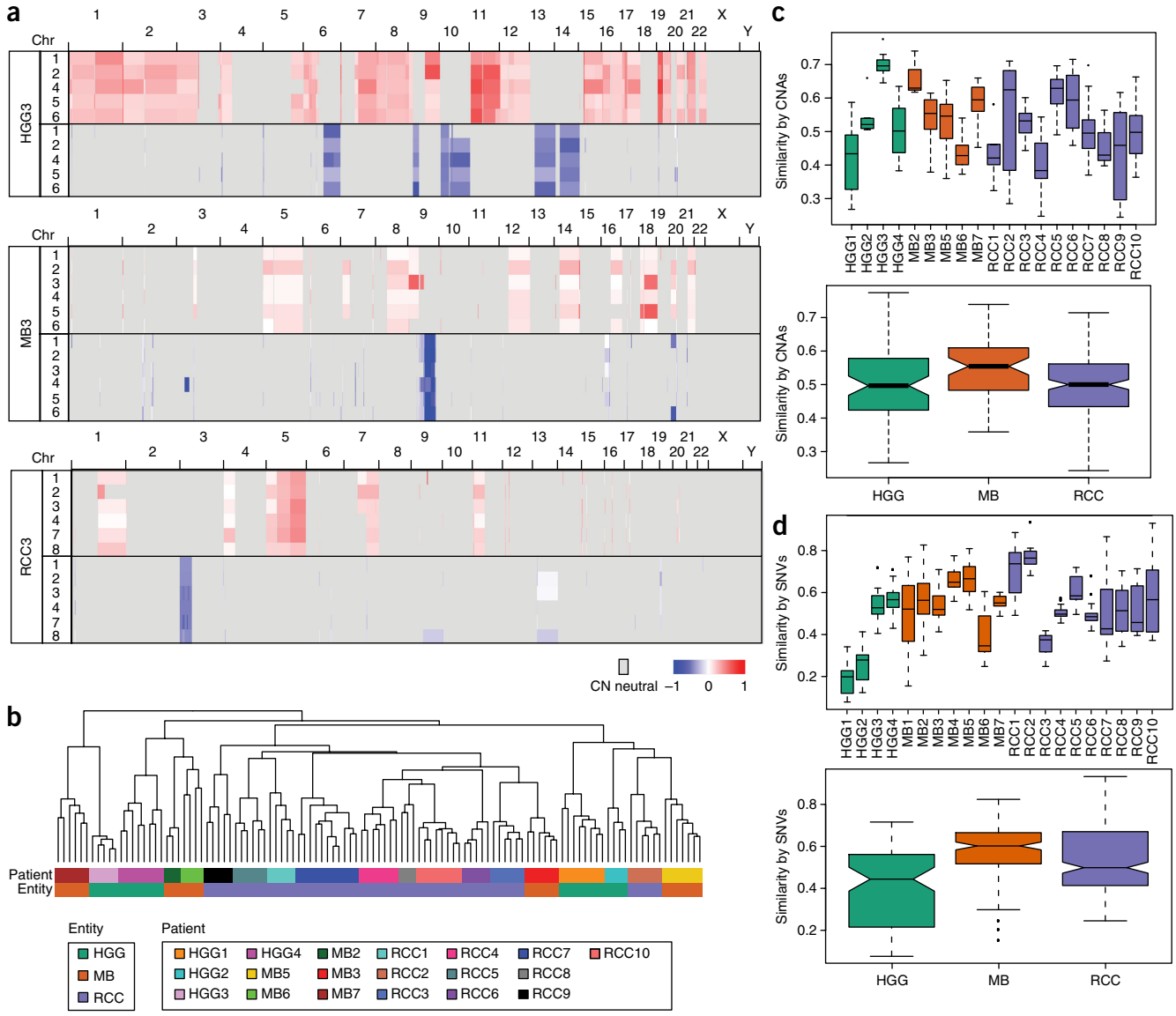

Figure 2 The variable intratumoral heterogeneity of somatic alterations in all tumor entities. Genome-wide analysis of CNAs did not recapitulate the striking expression-based spatial homogeneity of MBs. (**a**) Copy-number (CN) segments of gain (red) and loss (blue) across the genomes of three individual patients for each biopsy. (**b**) Unsupervised HCL of copy-number segments shows tight clustering of individual biopsies across all tumors in the cohort. (**c**,**d**) The intratumoral heterogeneity measured from CNAs (**c**; $n = 19$) or SNVs (**d**; $n = 21$), both in individual patients (top) and summarized by entity (bottom), shows that tumors in all entities range from high (e.g., HGG3 and MB2) to low (e.g., HGG1 and RCC3) spatial similarity. Similarity was measured as the binary distance between all pairs of tumor-matched biopsies. Box plot center lines indicate data medians; box limits indicate the 25th and 75th percentiles; whiskers extend 1.5 times the interquartile range from the 25th and 75th percentiles; outliers are represented by individual points. Notches in box plots (the lower plots in **c**,**d**) indicate where the 95th percentile of the data falls.

This genomic complexity results from a process of clonal evolution whereby the successive acquisition of mutations and CNAs generates genetically related subpopulations of cells or lineages within each tumor. We integrated CNA and mutational data using the EXPANDS algorithm[22], to infer the cellular lineage composition in each biopsy. EXPANDS detects multiple genetically distinct coexisting subpopulations of cells and allows phylogenetic reconstruction of their evolutionary relationships. **Figure 3a**, which describes the spatial distribution of genetically distinct subpopulations throughout a tumor, illustrates the clonal intermixing detected in many samples of the cohort (**Fig. 3b–d**, **Supplementary Fig. 10**, **Supplementary Table 1e**,**f**). Many tumor biopsies had a major clone (i.e., a genotype present in >70% of tumor cells) that was also detected in a minority of cells in other biopsies from the same tumor (i.e., subclonal) or that was absent in other biopsies (for example, biopsies 3, 5, and 6 from tumor RCC7 were genetically similar to some cells in biopsy 4 (4a), but not all cells (4b clustered separately); **Fig. 3c**). In some tumors, individual biopsies contained two or more cell lineages that independently accumulated distinct repertoires of mutations not found elsewhere in the tumor (e.g., HGG2 biopsies 1 and 5; **Fig. 3c**). The presence of multiple genetically distinct cellular lineages within single biopsies has previously been linked to poor prognosis and treatment response across a variety of cancer types[23].

This surprising but common pattern of major genetic clones in one biopsy that are subclonal or absent in spatially distinct locations in the same tumor prompted us to investigate observable mutation clonality

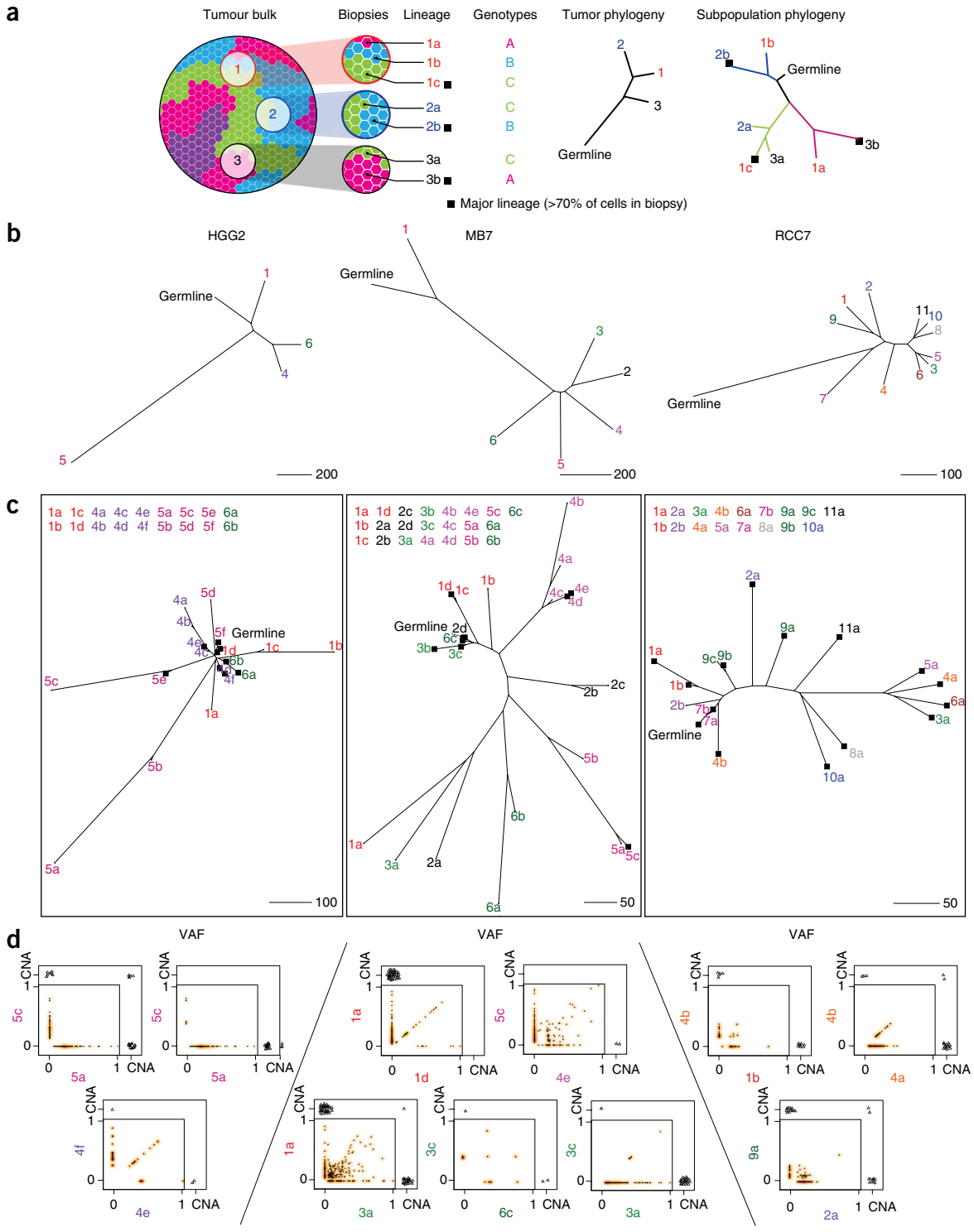

Figure 3 Spatial intermixing of clonal lineages. (**a**) Example illustration of a tumor with four clonal lineages that are spatially dispersed (color-coded in blue, green, pink, and purple), demonstrating how data from three biopsies can be used to build a typical biopsy-level phylogenetic tree as well as a subpopulation-level tree that reflects intermixing of the three detected genetic lineages. Branch tips are color-coded according to biopsy number, and labeled according to biopsy number (1, 2, 3) and clonal lineage (a, b, c). Branch colors correspond to the cellular genotype; black squares indicate major cellular lineages (>70% of tumor cells in the biopsy, scaled by the largest detectable population). Note that the number of biopsies may not be sufficient to 'discover' all distinct clonal lineages (e.g., purple clone). (**b**) Biopsy-level trees of three representative tumors: HGG2, MB7, and RCC7. (**c**) Subpopulation-level trees showing that some cellular lineages have high similarity to lineages in other biopsies, thus suggesting spatial intermixing (e.g., MB7 biopsies 1, 2, and 3; RCC7 biopsy 4). Conversely, some biopsies harbored more than one distinct lineage (e.g., HGG2 biopsy 5). (**d**) Variant allele frequencies (VAFs) of mutations are shown along with CNAs exclusive to or shared by pairs of biopsies or subpopulations. VAF scatter plots have a smoothed color density; black dots represent individual mutations. CNA events (triangles) are shown (with some jitter) if they were present in either compartment, or shared.

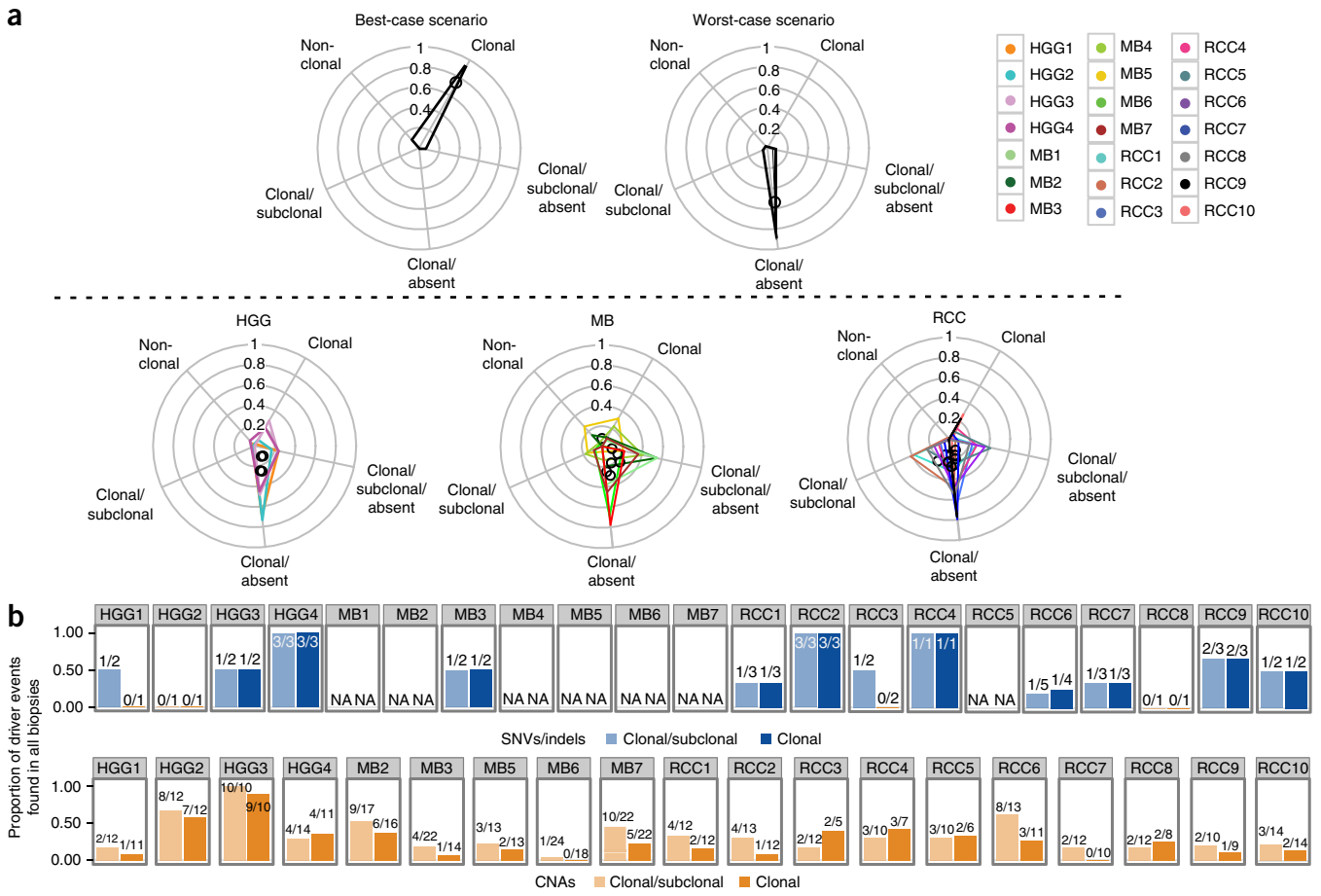

Figure 4 Genetically distinct clonal lineages yield ON/OFF mutation patterns between spatially separated biopsies. (**a**) Nonsynonymous mutations binned into five categories: clonal in all biopsies (clonal); clonal in some biopsies and subclonal in others (clonal/subclonal); clonal in some biopsies and completely absent in others (clonal/absent); clonal in some biopsies, and subclonal or absent in others (clonal/subclonal/absent); and never detected as clonal (non-clonal). Top, illustration of the most favorable clinical scenario, in which most mutations are clonal across all biopsies (left), and the worst-case scenario, in which mutations are clonal in some biopsies but absent in others (right). Bottom, mutation patterns follow a worst-case scenario across tumor types. Tumor-specific polygons on radial plots indicate the proportion of mutations on each of the five axes, with polygon centers marked by black circles. (**b**) The proportion of driver mutations/indels (top) or CNAs (bottom) that are found in every biopsy of a given tumor (i.e., trunk events) when both clonal and subclonal or only clonal driver events are considered. The absolute numbers are shown above the bars.

across biopsies, as clonality is a key requirement of clinically actionable therapeutic targets[24]. We classified mutations into clonal and subclonal populations (**Supplementary Fig. 11**, **Supplementary Table 1g**) and determined whether the status of the subset of damaging clonal mutations changed between spatially separated tumor biopsies. In nearly all tumors we found a predominance of clonal mutations that were subclonal or completely absent in additional biopsies (**Fig. 4a**, **Supplementary Fig. 12**; validation set of seven mutations with a 96% validation rate across biopsies; **Supplementary Fig. 13**, **Supplementary Table 1h**). This observation held when we considered only driver events[25–28] (**Fig. 4b**, **Supplementary Table 1i–k**). We predict that monotherapies against a single target identified in a single biopsy are unlikely to show dramatic clinical effects, as targets are not ubiquitous; this would leave untargeted clones in unsampled portions of the tumor free to survive and repopulate the tumor.

When the goal of a cancer therapy is improved patient treatment, the clinically relevant question is whether the observed level of genomic spatial heterogeneity affects actionable or driver alterations. As proof of concept, we focused on a set of genes with known roles in cancer initiation and/or progression[29], or with defined drug interactions[30]. These genes are enriched in relevant or actionable targets in a manner that is unbiased toward either of the cancer types we included (**Supplementary Table 1l,m**). When we investigated the spectrum of SNVs, indels, and CNAs affecting these genes (**Supplementary Figs. 14** and **15**), we found a remarkable variety of patterns across tumors, including cases with only a small set of shared alterations across biopsies but with many events present in single biopsies (e.g., *MET* amplification in HGG4); homogeneous tumors with many shared actionable events (e.g., HGG3); cases without ubiquitous actionable targets, which may require multiagent targeted therapeutics (e.g., MB6); tumors that lacked vulnerability to any of the considered actionable targets in a subset of biopsies (e.g., MB7); and tumors with alterations that may predict resistance (e.g., *TP53* compound loss and somatic mutation in RCC7).

Considering the full set of identified actionable mutations per tumor across all biopsies, we calculate that in each tumor entity, an average of at least five biopsies is required to provide an 80% chance of identifying at least 80% of these alterations. If these measures were reduced to 50%, sampling of at least two biopsies would be required, or as many as four for highly heterogeneous tumors (**Fig. 5a**). This is probably an underestimation, as the detection of actionable mutations does not plateau in most patients (**Supplementary Fig. 16**).

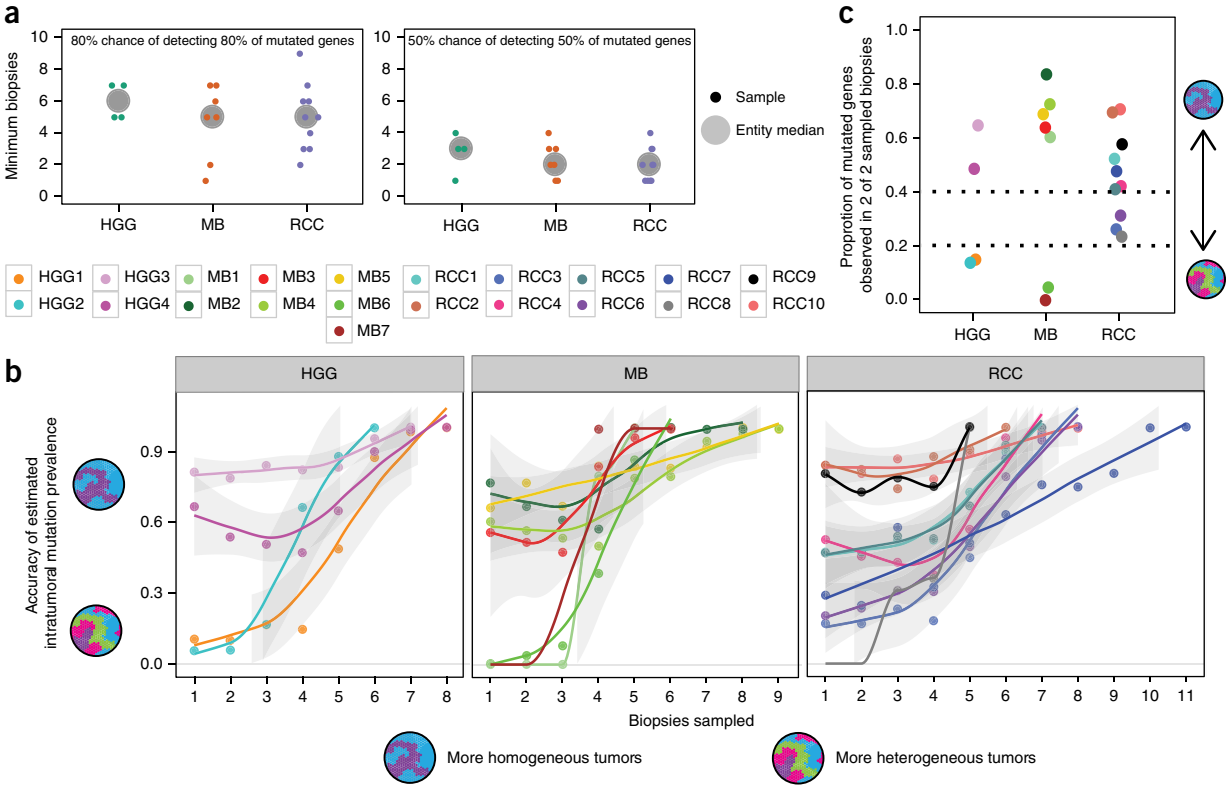

Figure 5 Quantification of variable genetic heterogeneity across tumor entities. (**a**) Our analysis of all mutated genes (from the list of actionable targets) identified in each tumor across all biopsies suggests that an average of five biopsies of an individual tumor is required to provide an 80% likelihood of recovering 80% of the known mutated genes (left). At least two biopsies are required to achieve a 50% likelihood of recovering 50% of mutated genes (right). (**b**) The likelihood of correctly inferring the frequency of a mutation in a whole tumor depends on the number of biopsies sampled, and whether the tumor is more or less genetically homogeneous. The accuracy of frequency prediction for brain tumors shows a bimodal pattern, with low-genetic-variance tumors having higher accuracy (>0.6) even with few biopsies, whereas at least five biopsies are required to achieve the same confidence in high-genetic-variance tumors (HGG and MB). RCCs additionally show an intermediate pattern. Accuracy was measured as the proportion of times that a gene's observed frequency in a selection of biopsies was within 10% of the known frequency across all biopsies. Lines represent a Loess fit to the points per tumor; gray shading indicates the 95% confidence interval. (**c**) Given a random selection of two biopsies, we ranked patients on the basis of the proportion of mutated genes (from the actionable target list) present in both biopsies. Patients with genetically heterogeneous tumors had median values < 0.2. Points represent the median value of all possible biopsy pairs per patient, and are color-coded according to the key in **a**.

Up-front profiling of numerous tumor regions to identify the full repertoire of actionable targets is neither practical nor likely, given the amount of sequencing required; thus we focused on maximizing the information derived from a minimal set of biopsies. Specifically, we wanted to determine how well we could predict the frequency of individual mutations across a tumor with an increasing number of biopsies, noting that prediction accuracy for mutations identified in a single fraction would be high only in very homogeneous tumors. We empirically determined the frequency of each alteration, considering all possible pairs of an increasing number of biopsies, and compared this observed quantity to the known frequency of the alteration in all biopsies; the difference between these values was the inference error of mutation frequency resulting from an insufficient number of biopsies from genetically heterogeneous tumors (**Supplementary Fig. 17**). Using a 10% error rate as an acceptable threshold, we calculated for each tumor the number of observed mutation frequencies that fell within this range (i.e., accuracy). As expected, we found that accuracy improved with increasing numbers of biopsies, and also that brain tumors fall into two patterns. The first comprises more homogeneous tumors, which have fairly high prediction accuracy even with a low number of biopsies, and the second comprises more heterogeneous tumors for which multiple biopsies are required to ensure an accurate determination of mutation frequency (**Fig. 5b**). In our cohort of MBs and glioblastomas, considering just two biopsies per tumor enabled the distinction of tumors with high versus low genetic heterogeneity, with high specificity especially for highly heterogeneous tumors (**Fig. 5c**, **Supplementary Fig. 18**).

Although spatial heterogeneity is clearly a barrier to highly effective therapeutics against an entire primary tumor, the extent of heterogeneity between primary and recurrent MB[31] is many fold greater (**Fig. 6a**, **Supplementary Fig. 19**). This vast discordance at relapse is therefore unlikely to be secondary solely to inadequate spatial sampling of the therapeutically naive primary tumor. In gliomas[32], the recurrent disease resembles the primary tumor more closely, and only in rare cases diverges to the extent seen in MB, possibly as a result of less complete success in the resection of this more diffuse and infiltrating tumor. MB is known to recur from very rare populations of cells[31]; thus, therapeutic approaches that can eradicate such cellular lineages despite their low prevalence in the primary tumor are severely needed.

Targeted cancer immunotherapy is based on the presence of tumor-specific cell-surface antigens, as opposed to cell-autonomous somatic mutations. We examined the expression of the antigens/genes for which chimeric antigen receptor T cells or monoclonal antibodies

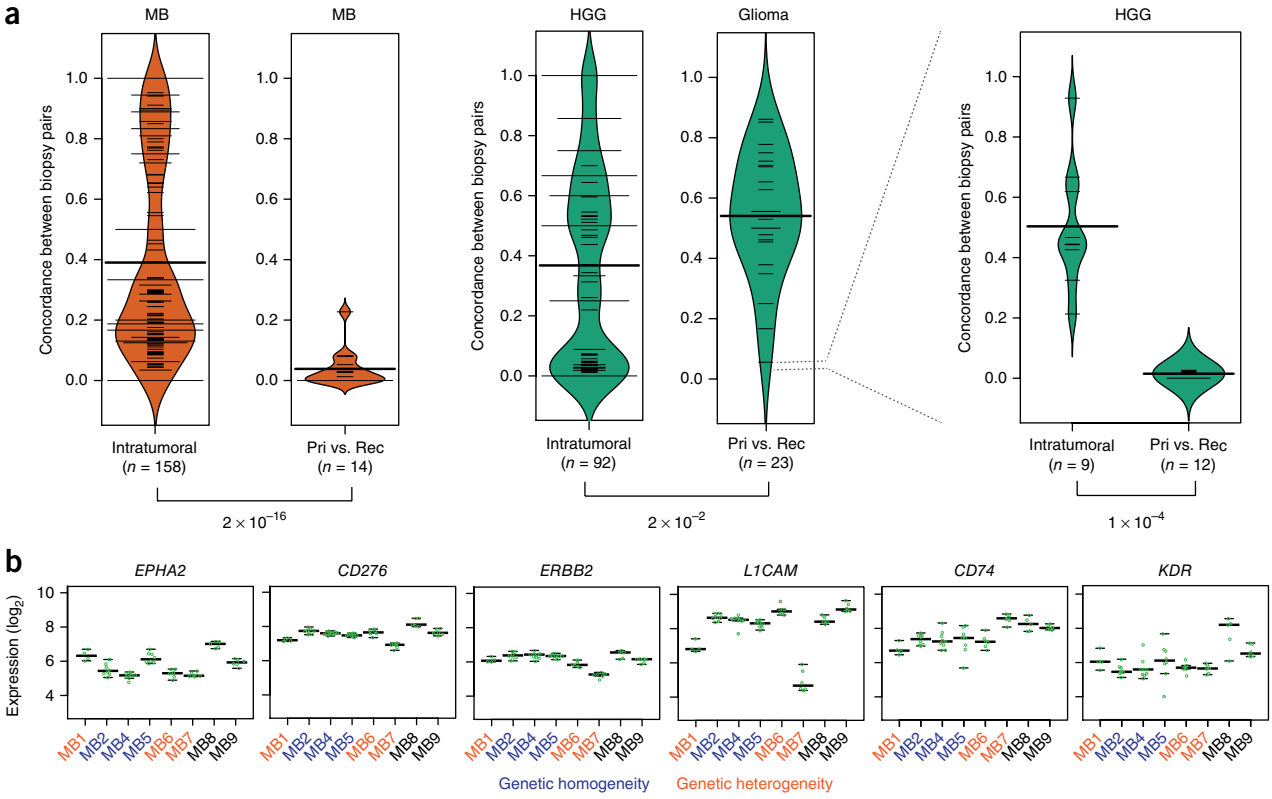

Figure 6 Genetic heterogeneity at recurrence greatly exceeds spatial heterogeneity in MB. (**a**) The genetic concordance of pre- versus post-therapy biopsies (data from ref. 31) was an order of magnitude lower than the up-front genetic spatial heterogeneity in MB samples ($P < 10^{-16}$, Welch two-sample *t*-test; $n = 14$ primary (Pri)–recurrence (Rec) pairs; $n = 158$ spatial comparisons from seven tumors). HGGs in our cohort showed a similar overall distribution of spatial heterogeneity ($n = 92$ comparisons from four tumors), and were not dramatically different compared with the low concordance of low-grade gliomas (LGGs) to HGGs post-therapy[41] ($n = 23$ glioma primary–recurrence pairs; data from ref. 32). One LGG relapse to HGG exhibited post-therapeutic genetic concordance values on par with those for MBs ($P < 10^{-4}$, Welch two-sample *t*-test; $n = 12$ primary–recurrence comparisons from patient 17 of ref. 32; $n = 9$ spatial comparisons). Concordance was measured as the proportion of clonal somatic mutations in common between a pair of biopsies, given the total number of clonal somatic mutations in the two samples. The width of the bean plots scales with the number of measurements with a similar *y*-value, showing data distribution. Thin horizontal lines indicate individual observations; multiple observations with the same value were added together to form wider lines. Thick horizontal bars indicate averages. (**b**) Low expression variance was observed across multiregion biopsies of cell-surface molecules with immunotherapies currently in clinical trials. This indicates that tumors with high genetic spatial heterogeneity may respond well to chimeric antigen receptor T cell or antibody-based therapy. Green points mark the expression of target genes in individual biopsies; horizontal lines indicate the median expression and the 25th and 75th percentiles of expression per tumor.

already exist[33–43], and we observed remarkable consistency of expression across multiregional biopsies, which contrasts sharply with the heterogeneity of somatic mutations across fractions in the same set of tumors. This was the case in all MBs examined, including those with high levels of genetic heterogeneity and for which targeted therapy would be problematic[33–43] (**Fig. 6b**, **Supplementary Fig. 20**). The homogeneity of the transcriptome versus the heterogeneity of somatic mutations in our MB cohort suggests that targeted immunotherapeutic approaches could potentially overcome the hurdle of spatial genetic heterogeneity.

The vast majority of patients with brain tumors have their tumor classified from a single tumor biopsy, which is potentially adequate for MB, but not for glioblastoma. The extent of the spatial heterogeneity of somatic mutations observed in our cohort suggests that clinical trials of molecularly targeted therapy should first assess the ubiquitous distribution of the target. The lack of clonal actionable driver mutations that are ubiquitously present across all regions of a given brain tumor suggests that monotherapies that target a single gene from a single biopsy are unlikely to have dramatic effects in terms of improving the lives of patients with brain tumors.

URLs. Gene Expression Omnibus, https://www.ncbi.nlm.nih.gov/geo/; European Genome-phenome Archive, https://www.ebi.ac.uk/ega/.

METHODS

Methods, including statements of data availability and any associated accession codes and references, are available in the online version of the paper.

Note: Any Supplementary Information and Source Data files are available in the online version of the paper.

ACKNOWLEDGMENTS

The MAGIC project (M.D.T. and M.A.M.) is financially supported by Genome Canada, Genome BC, Terry Fox Research Institute, Ontario Institute for Cancer Research, Pediatric Oncology Group Ontario, funds from The Family of Kathleen Lorette and the Clark H. Smith Brain Tumour Centre, Montreal Children's Hospital Foundation, Hospital for Sick Children: Sonia and Arthur Labatt Brain Tumour Research Centre, Chief of Research Fund, Cancer Genetics Program, Garron Family Cancer Centre, B.R.A.I.N. Child, M.D.T.'s Garron Family Endowment, and the BC Childhood Cancer Parents Association. M.D.T. is supported by a Stand Up To Cancer St. Baldrick's Pediatric Dream Team Translational Research Grant (SU2C-AACR-DT1113); Stand Up To Cancer is a program of the Entertainment Industry Foundation administered by the American Association for Cancer

Research. M.D.T. is also supported by The Garron Family Chair in Childhood Cancer Research, and grants from the Cure Search Foundation, the US National Institutes of Health (R01CA148699 and R01CA159859), The Pediatric Brain Tumor Foundation, The Terry Fox Research Institute, and Brainchild. This study was conducted with the support of the Ontario Institute for Cancer Research through funding provided by the Government of Ontario, as well as The Brain Tumour Foundation of Canada Impact Grant of the Canadian Cancer Society and Brain Canada with the financial assistance of Health Canada (grant 703202 to M.D.T.). This work was also supported by a Program Project Grant from the Terry Fox Research Institute (to M.D.T.), a Grand Challenge Award from CureSearch for Children's Cancer (to M.D.T.), and the PedBrain Tumor Project contributing to the International Cancer Genome Consortium, funded by German Cancer Aid (109252) and by the German Federal Ministry of Education and Research (BMBF; grants 01KU1201A and MedSys 0315416C to S.M.P. and P.L.). We acknowledge the Labatt Brain Tumour Research Centre Tumour and Tissue Repository, which is supported by B.R.A.I.N. Child and Megan's Walk (M.D.T.). M.A.M. acknowledges support from the Canadian Institutes of Health Research (CIHR; FDN-143288). M.R. is supported by a fellowship from the Dr. Mildred Scheel Foundation for Cancer Research/German Cancer Aid. F.M.G.C. is supported by the Stephen Buttrum Brain Tumour Research Fellowship, granted by the Brain Tumour Foundation of Canada. V.R. is supported by a CIHR fellowship and an Alberta Innovates–Health Solutions Clinical Fellowship. For technical support and expertise in next-generation sequencing efforts, we thank The Centre for Applied Genomics (Toronto, Ontario, Canada). We thank S. Archer for technical writing, and C. Smith for artwork.

AUTHOR CONTRIBUTIONS

A.S.M., F.M.G.C., M.R., M.D.T., and M.A.M. led the study and wrote the manuscript. A.S.M. and F.M.G.C. designed, supervised, and performed bioinformatic analyses. M.R. led the collection of samples and data generation, and performed bioinformatic analyses. B.L. extracted nucleic acids, managed biobanking, and maintained the patient database. S.H., A.M.F., B.L.H., C.D., D.J.H.S., D.M.M., D.P., D.T.W.J., E.N.K., H.F., J.M., J.P., J.R., J.T., L.G., L.K.D., M.V., P.A.N., S. Agnihotri, S. Albrecht, S.C.M., S.P.-C., V.H., V.R., X. Wu, X. Wang, and Y.Y.T. provided technical and bioinformatic support. A.A., A.T., C.M., D.L., E.C., E.M., H.I.L., J.E.S., K.T., M.M., N.D., P.P., R.C., R.D.C., T.W., W.L., Y.C., and Y.L. led and performed RNA-seq and whole-genome sequencing library preparation and sequencing experiments, and performed data analyses. N.T. and Y.M. supervised bioinformatic analyses at the Genome Sciences Center. H.N. and T.G. performed whole-exome sequencing library preparation and sequencing experiments, and performed data analyses. B.R.R., C.S., C.E.H., J.L., J.S.M., N.J., P.B., R.J.P., S.D., and U.S. provided the patient samples and clinical details that made the study possible. A.H., A.J.M., A.K., D.M., E.B., G.D.B., J.T.R., M.K., P.D., P.L., R.A.M., S.J.M.J., S.M.P., and U.T. provided valuable input regarding study design, data analysis, and interpretation of results. M.D.T. and M.A.M. provided financial and technical infrastructure and oversaw the study, and served as joint senior authors and project co-leaders.

COMPETING FINANCIAL INTERESTS

The authors declare no competing financial interests.

1. Northcott, P.A. *et al.* Medulloblastoma comprises four distinct molecular variants. *J. Clin. Oncol.* **29**, 1408–1414 (2011).
2. Kleinman, C.L. *et al.* Fusion of TTYH1 with the C19MC microRNA cluster drives expression of a brain-specific DNMT3B isoform in the embryonal brain tumor ETMR. *Nat. Genet.* **46**, 39–44 (2014).
3. Versteege, I. *et al.* Truncating mutations of hSNF5/INI1 in aggressive paediatric cancer. *Nature* **394**, 203–206 (1998).
4. Pietsch, T. *et al.* Prognostic significance of clinical, histopathological, and molecular characteristics of medulloblastomas in the prospective HIT2000 multicenter clinical trial cohort. *Acta Neuropathol.* **128**, 137–149 (2014).
5. Remke, M., Ramaswamy, V. & Taylor, M.D. Medulloblastoma molecular dissection: the way toward targeted therapy. *Curr. Opin. Oncol.* **25**, 674–681 (2013).
6. Kool, M. *et al.* Genome sequencing of SHH medulloblastoma predicts genotype-related response to smoothened inhibition. *Cancer Cell* **25**, 393–405 (2014).
7. Kieran, M.W. Targeted treatment for sonic hedgehog-dependent medulloblastoma. *Neuro-oncol.* **16**, 1037–1047 (2014).
8. Louis, D.N. *et al.* The 2007 WHO classification of tumours of the central nervous system. *Acta Neuropathol.* **114**, 97–109 (2007).
9. Gerlinger, M. *et al.* Genomic architecture and evolution of clear cell renal cell carcinomas defined by multiregion sequencing. *Nat. Genet.* **46**, 225–233 (2014).
10. Gerlinger, M. *et al.* Intratumor heterogeneity and branched evolution revealed by multiregion sequencing. *N. Engl. J. Med.* **366**, 883–892 (2012).
11. Gulati, S. *et al.* Systematic evaluation of the prognostic impact and intratumour heterogeneity of clear cell renal cell carcinoma biomarkers. *Eur. Urol.* **66**, 936–948 (2014).
12. Sottoriva, A. *et al.* Intratumor heterogeneity in human glioblastoma reflects cancer evolutionary dynamics. *Proc. Natl. Acad. Sci. USA* **110**, 4009–4014 (2013).
13. Verhaak, R.G. *et al.* Integrated genomic analysis identifies clinically relevant subtypes of glioblastoma characterized by abnormalities in PDGFRA, IDH1, EGFR, and NF1. *Cancer Cell* **17**, 98–110 (2010).
14. Taylor, M.D. *et al.* Molecular subgroups of medulloblastoma: the current consensus. *Acta Neuropathol.* **123**, 465–472 (2012).
15. Northcott, P.A. *et al.* Enhancer hijacking activates GFI1 family oncogenes in medulloblastoma. *Nature* **511**, 428–434 (2014).
16. Northcott, P.A. *et al.* Subgroup-specific structural variation across 1,000 medulloblastoma genomes. *Nature* **488**, 49–56 (2012).
17. Vanner, R.J. *et al.* Quiescent sox2^{+} cells drive hierarchical growth and relapse in sonic hedgehog subgroup medulloblastoma. *Cancer Cell* **26**, 33–47 (2014).
18. Beuselinck, B. *et al.* Molecular subtypes of clear cell renal cell carcinoma are associated with sunitinib response in the metastatic setting. *Clin. Cancer Res.* **21**, 1329–1339 (2015).
19. Thibodeau, B.J. *et al.* Characterization of clear cell renal cell carcinoma by gene expression profiling. *Urol. Oncol.* **34**, 168.e1–168.e9 (2016).
20. Gravendeel, L.A. *et al.* Intrinsic gene expression profiles of gliomas are a better predictor of survival than histology. *Cancer Res.* **69**, 9065–9072 (2009).
21. Ha, G. *et al.* TITAN: inference of copy number architectures in clonal cell populations from tumor whole-genome sequence data. *Genome Res.* **24**, 1881–1893 (2014).
22. Andor, N., Harness, J.V., Müller, S., Mewes, H.W. & Petritsch, C. EXPANDS: expanding ploidy and allele frequency on nested subpopulations. *Bioinformatics* **30**, 50–60 (2014).
23. Andor, N. *et al.* Pan-cancer analysis of the extent and consequences of intratumor heterogeneity. *Nat. Med.* **22**, 105–113 (2016).
24. Hiley, C., de Bruin, E.C., McGranahan, N. & Swanton, C. Deciphering intratumor heterogeneity and temporal acquisition of driver events to refine precision medicine. *Genome Biol.* **15**, 453 (2014).
25. Northcott, P.A. *et al.* Medulloblastomics: the end of the beginning. *Nat. Rev. Cancer* **12**, 818–834 (2012).
26. Sturm, D. *et al.* Paediatric and adult glioblastoma: multiform (epi)genomic culprits emerge. *Nat. Rev. Cancer* **14**, 92–107 (2014).
27. Shih, D.J. *et al.* Cytogenetic prognostication within medulloblastoma subgroups. *J. Clin. Oncol.* **32**, 886–896 (2014).
28. Linehan, W.M. *et al.* Comprehensive molecular characterization of papillary renal-cell carcinoma. *N. Engl. J. Med.* **374**, 135–145 (2016).
29. Futreal, P.A. *et al.* A census of human cancer genes. *Nat. Rev. Cancer* **4**, 177–183 (2004).
30. Griffith, M. *et al.* DGIdb: mining the druggable genome. *Nat. Methods* **10**, 1209–1210 (2013).
31. Morrissy, A.S. *et al.* Divergent clonal selection dominates medulloblastoma at recurrence. *Nature* **529**, 351–357 (2016).
32. Johnson, B.E. *et al.* Mutational analysis reveals the origin and therapy-driven evolution of recurrent glioma. *Science* **343**, 189–193 (2014).
33. Geldres, C. *et al.* T lymphocytes redirected against the chondroitin sulfate proteoglycan-4 control the growth of multiple solid tumors both in vitro and in vivo. *Clin. Cancer Res.* **20**, 962–971 (2014).
34. Stein, R. *et al.* CD74: a new candidate target for the immunotherapy of B-cell neoplasms. *Clin. Cancer Res.* **13**, 5556s–5563s (2007).
35. Wu, M.R., Zhang, T., DeMars, L.R. & Sentman, C.L. B7H6-specific chimeric antigen receptors lead to tumor elimination and host antitumor immunity. *Gene Ther.* **22**, 675–684 (2015).
36. Chinnasamy, D. *et al.* Gene therapy using genetically modified lymphocytes targeting VEGFR-2 inhibits the growth of vascularized syngenic tumors in mice. *J. Clin. Invest.* **120**, 3953–3968 (2010).
37. Craddock, J.A. *et al.* Enhanced tumor trafficking of GD2 chimeric antigen receptor T cells by expression of the chemokine receptor CCR2b. *J. Immunother.* **33**, 780–788 (2010).
38. Hong, H. *et al.* Diverse solid tumors expressing a restricted epitope of L1-CAM can be targeted by chimeric antigen receptor redirected T lymphocytes. *J. Immunother.* **37**, 93–104 (2014).
39. Kakarla, S. *et al.* Antitumor effects of chimeric receptor engineered human T cells directed to tumor stroma. *Mol. Ther.* **21**, 1611–1620 (2013).
40. Lanitis, E. *et al.* Primary human ovarian epithelial cancer cells broadly express HER2 at immunologically-detectable levels. *PLoS One* **7**, e49829 (2012).
41. Pule, M.A. *et al.* Virus-specific T cells engineered to coexpress tumor-specific receptors: persistence and antitumor activity in individuals with neuroblastoma. *Nat. Med.* **14**, 1264–1270 (2008).
42. Tang, X. *et al.* T cells expressing a LMP1-specific chimeric antigen receptor mediate antitumor effects against LMP1-positive nasopharyngeal carcinoma cells in vitro and in vivo. *J. Biomed. Res.* **28**, 468–475 (2014).
43. Wang, W. *et al.* Specificity redirection by CAR with human VEGFR-1 affinity endows T lymphocytes with tumor-killing ability and anti-angiogenic potency. *Gene Ther.* **20**, 970–978 (2013).

[1]Developmental & Stem Cell Biology Program, The Hospital for Sick Children, Toronto, Ontario, Canada. [2]The Arthur and Sonia Labatt Brain Tumour Research Centre, The Hospital for Sick Children, Toronto, Ontario, Canada. [3]Department of Pediatric Oncology, Hematology, and Clinical Immunology, Medical Faculty, University Hospital Düsseldorf, Düsseldorf, Germany. [4]Department of Neuropathology, Medical Faculty, University Hospital Düsseldorf, Düsseldorf, Germany. [5]Department of Pediatric Neuro-Oncogenomics, German Cancer Consortium (DKTK) and German Cancer Research Center (DKFZ), Düsseldorf, Germany. [6]Division of Haematology/Oncology, Department of Pediatrics, The Hospital for Sick Children, Toronto, Ontario, Canada. [7]Department of Laboratory Medicine and Pathobiology, University of Toronto, Toronto, Ontario, Canada. [8]Cancer Research Program, McGill University Health Centre Research Institute, Montreal, Quebec, Canada. [9]MacFeeters-Hamilton Brain Tumour Centre, Princess Margaret Cancer Centre, University Health Network, Toronto, Ontario, Canada. [10]Division of Neurosurgery, The Hospital for Sick Children, Toronto, Ontario, Canada. [11]Canada's Michael Smith Genome Sciences Centre, BC Cancer Agency, Vancouver, British Columbia, Canada. [12]Departments of Pediatrics and Human Genetics, McGill University, Montreal, Quebec, Canada. [13]Program in Genetics and Genome Biology, The Hospital for Sick Children, Toronto, Ontario, Canada. [14]Cancer Research UK London Research Institute, London, UK. [15]Division of Molecular Genetics, German Cancer Research Center (DKFZ), Heidelberg, Germany. [16]Division of Pediatric Neurooncology, German Cancer Research Center (DKFZ), Heidelberg, Germany. [17]Informatics and Biocomputing, Ontario Institute for Cancer Research, Toronto, Ontario, Canada. [18]Department of Medical Biophysics, University of Toronto, Toronto, Ontario, Canada. [19]The Donnelly Centre, University of Toronto, Toronto, Ontario, Canada. [20]Department of Pathology, Montreal Children's Hospital, McGill University Health Centre, Montreal, Quebec, Canada. [21]Division of Experimental Medicine, McGill University, Montreal, Quebec, Canada. [22]Division of Pathology, The Hospital for Sick Children, Toronto, Ontario, Canada. [23]Division of Pediatric Oncology, Children's National Medical Center, Washington, DC, USA. [24]Division of Pediatric Neuro-Surgery, Children's National Medical Center, Washington, DC, USA. [25]Department of Neurology, Children's National Medical Center, Washington, DC, USA. [26]Clinical Cooperation Unit Neuropathology, German Cancer Research Center (DKFZ), Heidelberg, Germany. [27]German Cancer Consortium (DKTK), Heidelberg, Germany. [28]Department of Pediatric Oncology, Hematology, Immunology and Pulmonology, University Hospital Heidelberg, Heidelberg, Germany. [29]Institute of Neuropathology, University Medical Center, Hamburg-Eppendorf, Germany. [30]Research Institute Children's Cancer Center, Hamburg, Germany. [31]Pediatric Hematology and Oncology, University Medical Center, Hamburg-Eppendorf, Germany. [32]Translational Cancer Therapeutics Laboratory, The Francis Crick Institute, London, UK. [33]Cancer Research UK Lung Cancer Centre of Excellence, University College London, London, UK. [34]Department of Medical Genetics, University of British Columbia, Vancouver, British Columbia, Canada. [35]Department of Molecular Biology & Biochemistry, Simon Fraser University, Burnaby, British Columbia, Canada. [36]Division of Neurosurgery, St. Michael's Hospital, University of Toronto, Toronto, Ontario, Canada. [37]These authors contributed equally to this work. Correspondence should be addressed to M.A.M. (mmarra@bcgsc.ca) or M.D.T. (mdtaylor@sickkids.ca).

ONLINE METHODS

Patients and samples. Multiregion tumor biopsies and clinical data were gathered for 35 tumors (9 primary medulloblastomas, 16 high-grade gliomas (10 with gene expression only[12]), and 10 renal cell carcinomas[10]); peripheral blood samples were included as germline controls for all cases with exome sequencing. All multiregion biopsies for unpublished cases were obtained *in situ* during tumor resection, by mimicking the previous sample-preparation conditions of published cases to the best of our knowledge. Medulloblastoma tumors are similar in size to glioblastomas, with an average diameter of 8–12 cm; biopsies were taken from regions as far apart as possible by the surgeon. Owing to their localization in the abdomen, renal cancers may be larger in size. Detailed information on multiregion tumor samples is provided in **Supplementary Table 1a** and **Supplementary Figure 1**. All patient material and clinical information was obtained after informed consent had been received and was approved by the institutional review boards of the contributing institutions. DNA and RNA extractions were performed as previously described[16]. RNA quality was assessed on a 2100 Bioanalyzer (Agilent Technologies, Santa Clara, CA). Only high-quality RNA (RNA integrity number ≥ 7) was included for further study.

Gene expression profiling. We carried out expression profiling on eight MB and three HGG multiregion biopsies, with a total of 72 biopsies and a median number of 6 multiregion biopsies per primary tumor (range: 4–9). We used Affymetrix HU133 Plus 2.0 microarrays for HGG samples, and Affymetrix Gene 1.1 ST arrays (Affymetrix, Santa Clara, CA) for MB samples, to ensure that these multiregion biopsies could be compared to published data sets[15–17,20]. Microarrays were processed according to the manufacturer's guidelines. Raw data were normalized with a transcript-level robust multi-array average (RMA) algorithm[44], and subsequently clustered by unsupervised HCL (Pearson's dissimilarity – average linkage) in Partek Genomics Suite. The molecular classification of the multiregion biopsy samples was done with the class-prediction algorithm PAM[45], as implemented in the pamr package (v. 1.51). Markers for glioblastoma (GBM) subtypes were obtained from the Verhaak classifier[13]. We note that classification was done for the GBM samples only, thus excluding HGG1. Subgroup-specific markers for MB were identified on the basis of one-way analysis of variance with multiple hypothesis correction by the Bonferroni method in previously published data sets with known subgroup affiliation[46]. On the basis of the misclassification error values in core GBM[13] and MB[15–17] training data sets (**Supplementary Fig. 6**), we chose threshold values of 1.75 and 1 for multiregion samples from published[12] and unpublished GBM and MB patient data, respectively. The published GBM data set[12] was quantile-normalized with Partek Genomics Suite. Predicted subtypes or subgroups with confidence probabilities higher than established thresholds[46] were considered *bona fide* subgroup assignments. Samples with less than 500 ng of remaining RNA were analyzed with NanoString as previously described[46]. MB3 was analyzed exclusively with NanoString, as only limited amounts of RNA were available for all multiregion biopsies. NanoString counts were normalized to the three housekeeping genes (*GAPDH*, *ACTB* and *LDHA*). We prepared dot plots and principal component analyses based on normalized NanoString calls using the R statistical environment (v2.15.1). Pearson correlation was used to determine the correlation of marker gene expression for each biopsy per patient (intratumor comparison) and between each biopsy and all others samples from different patients of the same subgroups (intertumor comparison). The Wilcoxon rank-sum test was used to infer differences in intra- and intertumor marker gene expression in a subgroup-specific fashion.

A previously published data set of nine multiregion RCC samples[9] profiled with the Affymetrix Human Gene 1.0 ST array was included in the analysis, as well as two RCC data sets[18,19] with 53 and 29 single RCC samples, respectively. The RCC expression data sets were processed together in R (v3.1.1) with the oligo package (rma normalization), and the combat package was used for batch-effect correction. Unsupervised HCL (Pearson's dissimilarity – average linkage) was carried out with the Partek Genomics Suite.

Whole-exome sequencing. DNA libraries (MB1–5) from multiregion samples were exome-captured with Agilent SureSelect V5+UTR probes and subjected to eight cycles of PCR, and then paired-end 75-base reads were sequenced over two lanes on an Illumina HiSeq 2000 instrument per pool of six libraries. Reads were aligned to the human reference genome hg19a with Burrows–Wheeler Aligner (BWA) (version 0.5.7)[47]. Two lanes were merged with duplicates marked with Picard Tools (version 1.71). Additional samples (MB6–7 and HGG1–5) were subjected to paired-end library construction using Illumina's Nextera Rapid Capture Exome kit. Captured exome DNA sequences were then sequenced with Illumina HiSeq 2000 (rapid-run mode) for 100-bp paired-end reads. We used the FASTX toolkit to remove adaptor sequences and to trim low-quality reads. Quality trimmed reads were then aligned to the human reference genome (hg19) using BWA (version 0.5.9)[47]. We used Genome Analysis Toolkit (GATK)[48] for indel realignment. We marked duplicate reads with Picard so we could exclude them further in our analysis.

Somatic SNV detection and filtering. SNVs were called exome-wide with SAMtools mpileup (v0.1.7), and indels were called with VarScan. We carried out stringent filtering requiring no reads in the germline sample supporting an SNV to ensure conservative selection of somatic events. Variants with sufficient coverage (≥10) were further annotated with Annovar[49] (table_annovar.pl; RefSeq gene annotations, amino acid change annotation, SIFT, PolyPhen, LRT, and MutationTaster scores, PhyloP and GERP++ conservation scores, dbSNP identifiers, 1000 Genomes Project allele frequencies, NHLBI-ESP 6500 exome project allele frequencies).

Mutation validation. We validated a subset of somatic mutations using PCR amplification from all tumor biopsies, matched germline, and a healthy control sample. We amplified regions of interest from genomic DNA with primers flanking each SNV (**Supplementary Table 1h,n**), using Q5 High-Fidelity DNA polymerase (NEB). PCR specificity was determined by agarose gel electrophoresis followed by gel extraction of specific bands using a Gel Extraction/PCR clean-up kit (Qiagen) according to the manufacturer's instructions. Purified amplicons were sequenced by Sanger sequencing, and traces were reviewed manually for the expected presence or absence of the mutated base.

Droplet digital PCR. For the validation and quantification of the frequency of the PIK3CA SNV detected in MB3, we used droplet digital PCR (ddPCR), as Sanger traces were of poor quality in the region of interest. We used genomic DNA from six spatially distinct biopsies from MB3, as well as matched germline and a healthy donor control, in the assay. We validated the *PIK3CA* mutation (chr 3:178936091 G>A) by using the PrimePCR ddPCR mutation assay kit, PIK3CA p.E545K, human (Bio-Rad; dHsaCP2000075 (mutant, FAM) and dHsaCP2000076 (wild-type, VIC)), according to the manufacturer's instructions. Fluorescence measurement with a QX100 ddPCR droplet reader (Bio-Rad) was used to detect the presence of mutant and wild-type alleles. QuantaSoft Analysis software (Bio-Rad) was used in the quantification.

Copy-number analysis. TITAN[21] estimates the cellular prevalence of tumor cell populations (lineages) on the basis of a user-defined number of clonal clusters, and user-defined ploidy estimation. Thus, we carried out 20 runs of TITAN for each exome, with cluster numbers 1–10 (representing one clonal lineage through to ten coexisting clonal lineages with distinct genotypes), and ploidy set to either 2 or 4. Copy-number segments from the 20 parameter combinations were analyzed and merged into larger segments if they were on the same chromosome arm, were <10 Mb apart, and had the same state (loss or gain). We compared merged results from each of the 20 parameter combinations for each biopsy in order to select the optimal parameter combination as the highest-scoring, considering the following criteria:

```
# maximize the largest contig size
# maximize the median contig size
# minimize the number of contigs
# minimize the number of clonal clusters
```

The parameter combination with the largest x value was selected as optimal:

$$x = ((L * M) * (M^2/10^9)^* (1/T)^* (1/(C+1)^2))/M/10^9$$

where L is the largest contig size (Gb), M is the median contig size (Gb), T is the total number of contigs, and C is the number of clonal clusters.

We next assessed the prevalence of copy-number segments (loss or gain) identified in the best parameter combination of a unique biopsy (i.e., target segments), using either all segments or clonal segments only (logratio ≥ |0.2|). A target segment was considered as found in another biopsy from the same tumor if any of the 20 parameter combinations contained a segment with the same state (loss or gain), and whose span had a minimum reciprocal overlap of at least 70% with the target segment.

Concordance of driver regions of loss and gain in the RCC tumor cohort was performed for our calls and the published data[9]. With our computational approach, we achieved 97% concordance compared with the manual curation performed previously[9], indicating that this method is specific and sensitive despite the high level of normal cell contamination in these tumors. Conversely, compared to our results for the subset of copy-number gains and losses identified in ref. 9, the manual curation showed 89% concordance to the TITAN pipeline, indicating that our approach is more sensitive, and that the homogeneity of certain copy-number driver events may be greater than previously estimated (**Supplementary Table 1c**). Finally, our approach is applicable genome-wide and across tumor types in a highly parallel fashion.

SNV classification using mclust. We classified variant allele frequencies (VAFs) of somatic SNVs into distinct clusters using the R package mclust[50], which uses finite mixture estimation via iterative expectation maximization steps and the Bayesian information criterion. Each cluster is manually categorized as 'homozygous', 'clonal', or 'subclonal', depending on the cluster VAF and the uncertainty separating it from the next cluster, and taking into account the biopsy tumor cell content value reported by TITAN. Multiple subclonal populations are numbered sequentially, starting with the most highly prevalent population. Clonal and subclonal mutation details per biopsy are summarized in **Supplementary Table 1d,g**.

Phylogenetic reconstruction from combined SNV and CNA data. We combined copy number and loss-of-heterozygosity (LOH) information derived from TITAN (including the clonal and subclonal events identified in the best parameter combination run for each biopsy), as well as somatic mutations and SNPs in areas of LOH, to infer tumor phylogenies using EXPANDS[22]. We ran EXPANDS v1.7.2 with the runExPANdS function. All parameters were set to default, with the exception of maxScore, which was lowered to 1.5 to reduce the false positive rate of subpopulation detection. Only subpopulations with a minimum size (cellular frequency) of 0.1 were considered. Mutations that could not be assigned to a high-confidence subpopulation were discarded, so that no ambiguous assignments were made. In addition, ambiguous subpopulations (i.e., groups of mutations and copy-number events) were dropped from the analysis. Mutations were assigned to all nested subpopulations (i.e., if a mutation was found in a subpopulation of cells at a high frequency of 0.8, it was also assigned to 'daughter' subpopulations of, for instance, frequency 0.5), to report the assignment of every mutation to all detected subpopulations in all biopsies of the tumor (assuming that the mutation could be assigned unambiguously as mentioned above; **Supplementary Table 1f**).

Phylogenetic relationships between the subpopulations inferred by the EXPANDS algorithm in all biopsies per patient were generated using both SNV and copy-number segments. The Manhattan distance metric was used to calculate pairwise distances between all pairs of biopsies on the basis of these data, and a complete linkage HCL was performed to generate phylogenies. Germline-rooted trees were generated with the as.phylo R function from the ape package.

Error inference of actionable genetic alterations. In order to analyze genetic heterogeneity affecting actionable and putative driver genes in a way that was unbiased toward any of the tumor types, we opted to use general lists of known cancer drivers and druggable targets. Sets of genes known to be drivers in GBM, MB, and RCC tumors come from studies of different cohort sizes, with sometimes unknown subgroup affiliations, and thus are not equally comprehensive. To overcome this, we used a list of genes of interest that included putative driver genes found in the Cancer Gene Census database[29] (n = 572) and actionable genes from the Drug-Gene Interaction Database[30] (n = 426 genes) (**Supplementary Table 1l,m**).

Oncoprint plots (R package ComplexHeatmap v1.6.0) were built for the combination list of these genes for all tumors, using (a) clonal mutations and indels and (b) clonal mutations and indels plus high-level CNAs (>4 copies gained; homozygous loss). A manual review of the results showed that the absence of clonal somatic mutations in subsets of biopsies is not explained by concordant copy-number loss. Because not all biopsies had copy-number data, we carried out further analyses using results from strategy (a) in order to maximize the number of usable biopsies per tumor.

Driver event lists. The MB CNA driver events listed in **Supplementary Table 1i,j** and **Figure 4b** were taken mainly from Shih *et al.*[27], with a subset of the mostly highly recurrent genes listed in Northcott *et al.*[25]. The HGG chromosome arm and recurrent driver gene events were retrieved from Tables 1 and 2 of ref. 26. RCC chromosome arm and gene-level driver events were retrieved from Supplementary Figure 2 (threshold FDR q-value < 10^{-15}) and Table S4 (q-value threshold: 0.05) of the ccRCC TCGA paper[28]. The cancer cell fraction values presented in **Supplementary Figure 10b** for driver mutations were calculated as previously described[51]:

$$\mathrm{CCF} = \mathrm{VAF}^{*}(1/\mathrm{Purity})(\mathrm{CN}^{*}\mathrm{Purity} + 2(1 - \mathrm{Purity}))$$

where CCF is the cancer cell fraction, VAF is the variant allele frequency, CN is the copy number at the mutation, and Purity is the tumor purity as calculated by EXPANDS.

Accuracy of mutation-frequency detection. We calculated the inferred error of the prevalence of each mutation across biopsies by using a subsampling approach. In each tumor, given a subset of biopsies from 1 to n (where n is the total number of biopsies per tumor), we calculated the frequency of each identified mutation in the biopsies sampled as f_o. We subtracted this value from the 'ground truth' expected frequency for that mutation across all n biopsies (f_e). When the observed and expected values were identical, then the inferred error ($f_e - f_o$) was 0. In the majority of tumors, there is a predominance of genes with mutations in single biopsies, leading to negative values of error for many genes, as the frequency of the mutation is often overestimated (**Supplementary Fig. 17**). In contrast, genes that are present in all but one or two biopsies will often have an error value greater than 0, as their frequency can be underestimated.

The likelihood of being within ±0.1 of 0 (i.e., close to perfect accuracy, given the data from all biopsies) is calculated as the proportion of genes at each sampling of 1:n biopsies where the error rate was within those bounds. For instance, we sampled all possible combinations of a certain number of biopsies from the total number of biopsies, and in each case calculated the inferred error of each detected mutation's prevalence. The proportion of the total set of error values < |0.1| represented the likelihood of a correct interpretation of mutation frequency given that number of biopsies (**Fig. 5b**).

Estimation of genetic heterogeneity from two biopsies. To address the practical issue of estimating genetic heterogeneity from a minimum number of informative biopsies, we implemented a simple metric of the proportion of mutated genes in a set of two biopsies that was ubiquitous (i.e., present in two of two biopsies). The mean value of all pairs of biopsies from a total of n biopsies per tumor showed a strong divergence in HGG and MB tumors, with high- versus low-variability tumors well separated (**Fig. 5c**). These were the same tumors that scored as high versus low variability on the basis of the accuracy metric described above.

We also observed clear separation of these two classes with the R package mclust (**Supplementary Fig. 18a**), which models univariate mixtures of Gaussian distributions (i.e., corresponding to a mixture of high- and low-genetic-variance brain tumors) via expectation maximization and the Bayesian information criterion[50]. Using two thresholds from the mclust density peaks (low, 0.55; high, 0.75), we calculated the accuracy of the classification of high-variance versus low-variance tumors on the basis of a single pair of biopsies, and observed that high-variance tumors in particular had high true positive and low false positive classification rates (**Supplementary Fig. 18b**). On the basis of this metric, the vast majority of pairs of biopsies from tumors with high genetic heterogeneity have a low percentage of gene mutations found in both biopsies, such that they are always classified as heterogeneous tumors, and almost never as homogeneous tumors.

doi:10.1038/ng.3838

Expression analysis of immunotherapeutic targets in MB tumors. Microarray expression data from the Affymetrix Gene 1.1 ST array (Affymetrix, Santa Clara, CA) for the MB samples were analyzed in the R environment (v3.1.1). We used the affy package (v1.44.0) and the custom CDF hugene11sthsensgcdf (v19.0.0) to summarize the expression of 21,641 Ensembl (ENSG) genes and process the data. Expression data were normalized via the rma method.

Spatial genetic variance versus post-treatment clonal evolution. To directly measure the relative contributions of spatial heterogeneity and clonal evolution induced by treatment, we used our previously published cohort of matched pre- and post-therapeutic MB samples[31]. This comparison showed that in MB, the amount of divergence observed between primary and relapse compartments far exceeded the spatial genetic variance in the primary tumor.

To assess whether the observed divergence between primary and recurrent MB is greater than the observed divergence between intratumoral biopsies, we reanalyzed the 14 primary–relapse tumor whole-genome sequencing (WGS) samples with matched germline, using the same pipeline as presented above. Briefly, mutations were called using SAMtools mpileup, filtered stringently against the germline, and shortlisted to those mutations with at least ten-reads coverage in both primary and recurrent samples, and are in areas of normal copy number and LOH. Because the samples in this work were exomes, we restricted the analysis of the primary–relapse samples to the same exonic regions. After removing the major analysis pipeline differences, we addressed differences in depth of coverage. The exome libraries were sequenced to an average of 60×, and the WGS samples were sequenced to 30× coverage. Thus, our ability to assess the similarity between regions in the exome libraries was more sensitive to subclonal events present at low levels (and therefore preferentially detectable by exome sequencing, and not by WGS). We addressed this bias by restricting the analysis to clonal events in the exomes, as clonal mutations are detectable in both exomes and genomes. To verify that this was a reasonable assumption, we compared the VAF of mutations found in the exomes to those found in matched WGS data generated from the same samples, but sequenced at 30× coverage. Matched WGS samples were available for biopsy 1 in each MB tumor with multiregional profiling. In all cases, we found that >75% of mutations with a VAF < 0.18 in the MB exomes were not found in the matched genomes sequenced from the same samples, which indicates that subclonal events are typically not well profiled at the shallower depths of a genomic library. Therefore, we restricted our analysis to clonal events in both exomes and genomes.

Focusing on the clonal and homozygous events detectable in both exome and genome data, we hypothesized that any differences between primary and relapse samples that were greater than the differences expected from different biopsies in a primary tumor would be largely attributable to clonal evolution as a consequence of therapy. To see whether the data supported this conclusion, we used the mutations in each biopsy to measure the pairwise concordance between all biopsies of individual tumors. Concordance was measured as the number of mutations in common between two biopsies, as a fraction of the total number of mutations present in both. In parallel, we used the mutations in the primary and relapse samples to measure pairwise concordance values between disease compartments. As a positive control, we compared the interbiopsy and intercompartmental concordance values of an adult GBM sample with multiple biopsies profiled before and after therapy (patient 17 from ref. 32).

In MB samples we found a mean pairwise concordance of 0.3903 between biopsies of the same tumor—nearly an order of magnitude higher than the mean concordance (0.03852) observed between disease compartments (Wilcoxon rank-sum test P value $< 2.2 \times 10^{-16}$). One sample stood out as an outlier (MB-REC-04), and we note that in that case the tumor was a group 4 local recurrence. This unusual pattern of recurrence for a group 4 tumor may indicate that the primary mass was sub-totally resected rather than grossly resected, thus explaining the higher similarity of the recurrent compartment to the primary.

In the case of the adult GBM patient (patient 17) with multiregionally sampled primary (three regions; low-grade glioma) and recurrent disease (four regions; high-grade glioma), we found the same trend: the primary–relapse mean concordance of 0.01506 was an order of magnitude smaller than the mean intrabiopsy concordance of 0.5036 (Wilcoxon rank-sum test P value = 0.0001406). There was no significant difference between the primary–relapse MB concordance and the primary–relapse GBM concordance observed in patient 17 (Wilcoxon rank-sum test P value = 0.5458). Similarly, there was no significant difference between the regional biopsies in GBM versus MB (Wilcoxon rank-sum test P value = 0.09926).

Finally, the primary–relapse divergence calculated from reprocessed data from patient 17 was on par with that initially presented in the glioma paper[41]; thus we included, for visual comparison, all the primary–relapse values for the glioma cohort in **Figure 6a** (middle panel; values directly derived from Supplementary Table 4 of ref. 32).

Statistical analysis. All statistical analyses were performed in the R statistical environment. Comparisons of categorical variables between entity types were done by two-sided Fisher's exact test. Comparisons of distributions were done by Welch two-sample t-test (parametric) or Wilcoxon rank-sum test (nonparametric). P values < 0.05 were considered statistically significant.

Data availability. The Gene Expression Omnibus accession codes for the previously unpublished gene expression data are GSE62802 (HGG samples) and GSE62803 (MB samples). The Toronto whole-exome sequencing data sets have been deposited in the European Genome-phenome Archive under accession codes EGAD00001000723 and EGAS00001001014.

44. Irizarry, R.A. *et al.* Summaries of Affymetrix GeneChip probe level data. *Nucleic Acids Res.* **31**, e15 (2003).
45. Tibshirani, R., Hastie, T., Narasimhan, B. & Chu, G. Diagnosis of multiple cancer types by shrunken centroids of gene expression. *Proc. Natl. Acad. Sci. USA* **99**, 6567–6572 (2002).
46. Northcott, P.A. *et al.* Rapid, reliable, and reproducible molecular sub-grouping of clinical medulloblastoma samples. *Acta Neuropathol.* **123**, 615–626 (2012).
47. Li, H. & Durbin, R. Fast and accurate short read alignment with Burrows-Wheeler transform. *Bioinformatics* **25**, 1754–1760 (2009).
48. McKenna, A. *et al.* The Genome Analysis Toolkit: a MapReduce framework for analyzing next-generation DNA sequencing data. *Genome Res.* **20**, 1297–1303 (2010).
49. Wang, K., Li, M. & Hakonarson, H. ANNOVAR: functional annotation of genetic variants from high-throughput sequencing data. *Nucleic Acids Res.* **38**, e164 (2010).
50. Fraley, C., Raftery, A., Murphy, T.B. & Scrucca,, L. *mclust Version 4 for R: Normal Mixture Modeling for Model-Based Clustering, Classification, and Density Estimation* (University of Washington, 2012).
51. Stephens, P.J. *et al.* The landscape of cancer genes and mutational processes in breast cancer. *Nature* **486**, 400–404 (2012).